Mechatronics 21 (2011) 908–917

Contents lists available at ScienceDirect

Mechatronics

journal homepage: www.elsevier.com/locate/mechatronics

The Distributed Flight Array

Raymond Oung *, Raffaello D'Andrea

Institute for Dynamic Systems and Control, ETH Zurich, 8092 Zurich, Switzerland

ARTICLE INFO

Article history:
Received 11 March 2010
Accepted 18 August 2010
Available online 4 May 2011

Keywords:
Aerial robotics
Distributed estimation and control
Multi-agent systems

ABSTRACT

The Distributed Flight Array is a multi-rotor vehicle that is being developed at ETH Zurich. This vehicle consists of autonomous single-rotor modules that are able to drive, dock with its peers, and fly in a coordinated fashion. These modules are organized as distributed computational units with minimal sensory input. Experimental demonstrations in docking, driving, and flying have proven its feasibility as a research platform for investigating techniques in distributed estimation and control.

1. Introduction

The Distributed Flight Array (DFA) is a multi-rotor vehicle that is being developed at the Institute for Dynamic Systems and Control at ETH Zurich. This vehicle consists of modules, each of which is equipped with a set of wheels that enable it to drive on the ground, and a fixed-pitch propeller that can generate enough thrust to lift itself into the air but is unstable in flight. Not until these modules are joined do these relatively simple devices evolve into a sophisticated multi-rotor system capable of coordinated flight. The goal of this project is to have many modules assemble at random, fly to a predetermined altitude, hover, break apart, fall back down, and then repeat the cycle in a new configuration, see Fig. 1 and Video 1 in Appendix: A.

This vehicle is to be used as a tool for research and education. As a research platform, the DFA can be used to effectively abstract many of the real-world issues that will be encountered when designing the next generation of distributed multi-agent systems. The rich dynamics and challenging design problems will motivate the development of fundamental algorithms and architectures for controlling systems with many interconnected components whose dynamics are not known precisely and/or change with time. Such algorithms and architectures may be used, for example, in cooperative slung payload systems [1] and high altitude airborne wind turbines [2] where modularity and high-redundancy is desirable in order to handle multiple points of failure while still remaining airborne. Unfortunately, such concepts in control theory are often difficult for the general public to appreciate, much less understand. Thus, the secondary function of the DFA is to illustrate control theory research in a tangible way to a mainstream audience.

This paper discusses the first steps taken towards developing this vehicle, and sets the foundation for future work. It summarizes three key aspects of the DFA – docking, driving, and coordinated flight – and presents experimental results for each. The paper begins with a detailed system description of a DFA module in Section 2. A drive model and flight model is then presented in Section 3. A docking strategy is summarized in Section 4 and an easily tunable strategy for hover control is described in Section 5. Experimental results are then presented in Section 6 and concluding remarks are made in Section 7.

2. Design

Recent experiments using the first revision of the modules shown in Fig. 2a have demonstrated feasibility of the DFA, which will be the focus of this paper. A second revision shown in Fig. 2b is currently in development and it will feature many improvements to the first revision.

The design challenges of the DFA mirror those of modular reconfigurable robots and micro aerial vehicles, which include electromechanical interconnection, inter-module communication, and energy storage [3–7]. The design of the system can be divided into four tightly interconnected sub-systems: (1) chassis and docking mechanism; (2) drive unit; (3) flight unit; and (4) sensing, communication and computation.

2.1. Chassis and docking mechanism

Each DFA module resembles a hexagon with protruding features designed for passive alignment and docking, see Fig. 2a.

* Corresponding author. Address: Institute for Dynamic Systems and Control, ETH Zurich, Sonneggstrasse 3, ML K 36.2, 8092 Zurich, Switzerland. Tel.: +41 44 632 69 64; fax: +41 44 632 11 39.
E-mail addresses: roung@ethz.ch (R. Oung), rdandrea@ethz.ch (R. D'Andrea).

0957-4158/$ - see front matter © 2010 Elsevier Ltd. All rights reserved.
doi:10.1016/j.mechatronics.2010.08.003

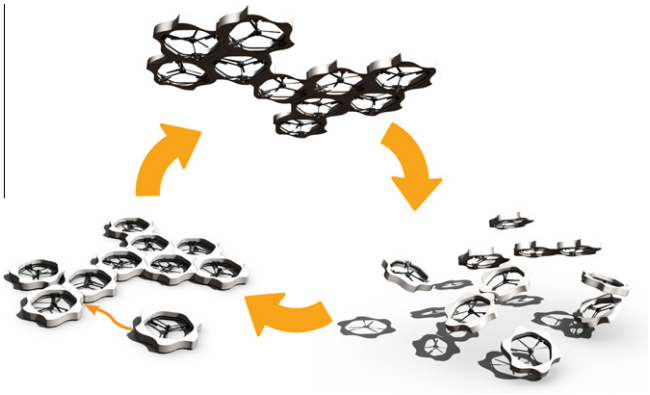

Fig. 1. This concept representation of the Distributed Flight Array (DFA) depicts the vehicle at different stages during its operating cycle. Starting from the lower left-hand corner of the figure, the modules assemble on the ground at random, generating a myriad of different possible network configurations. Once assembled, the modules coordinate and fly to a predetermined altitude and hover. After a certain amount of time, the modules break apart and fall back to the ground only to repeat the cycle in a new configuration.

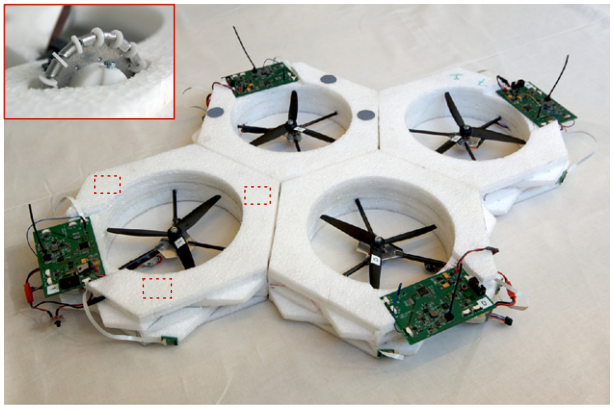

Fig. 2a. Four DFA modules (rev. 1) are shown in a docked configuration. The module's hexagonal chassis has protruding features designed for passive alignment and docking; it is assembled from foam sheet cutouts of low-density expanded polypropylene (EPP) foam. Mounted at the center of the chassis is a brushless DC motor and a 3-blade fixed-pitch propeller. The top-left inset shows a custom-made omnidirectional wheel; three of these wheels, their locations indicated by the dotted boxes around the chassis, are used to drive the module on the ground.

The chassis must be light enough to facilitate flight, and durable enough to repeatedly withstand a fall from at least 2 m. To accomplish this, a low-density expanded polypropylene foam was chosen as the chassis material [8,9]. Two-dimensional foam cut-outs were layered on top of one another to generate the assemblies shown in Figs. 2a and b. This relatively simple manufacturing process saves time and cost. However, it removes the possibility of generating a smooth leading edge for the duct which could improve thrust efficiency.

The protruding features assist with alignment and eliminate the unnecessary complexity of an active docking mechanism. A symmetric arrangement of four permanent magnets on each side of the module help to keep the modules attached. The magnets have been chosen to be strong enough to keep the modules together and to withstand the stresses of flight, but weak enough to break apart when a sufficient amount of force and/or torque is applied by a module.

Table 1 lists some of the important physical attributes that characterize a DFA module.

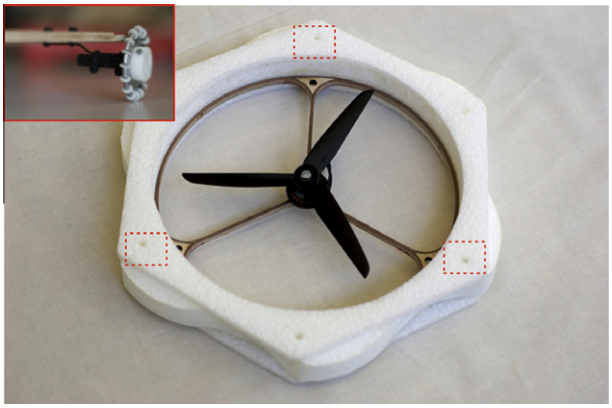

Fig. 2b. The next revision of the DFA module (rev. 2) may feature a new and improved EPP foam chassis with the on-board electronics embedded in the chassis for protection against impact. Also embedded in the foam chassis are the drive units, their locations indicated by the dotted boxes and shown in the top-left inset. The drive motor may be mounted to a cantilever spring suspension in order to absorb shock upon impact and prevent damage to the drive unit.

Table 1
Physical attributes of a DFA module (rev. 1).

Symbol	Description	Value
ℓ	Characteristic length[a]	0.250 m
r_w	Wheel distance[b]	0.100 m
–	Rotor duct diameter	0.180 m
m	Total mass	0.180 kg

[a] Defined as the distance between opposite sides of a module.
[b] Defined as the lateral distance from the center of the module to the center of the wheel.

2.2. Drive unit

Custom-made omnidirectional wheels with rollers orthogonal to the axis of the wheel are mounted to three sides of the chassis, see top-left insets of Figs. 2a and b. A 0.5 W brushed DC motor with integrated encoder for velocity feedback drives each wheel. Omni wheels were chosen because they offer a high degree of in-plane maneuverability, and they eliminate any steering linkage(s) that would otherwise be necessary for coordinated driving, as demonstrated in Section 6.2.

2.3. Flight unit

Mounted at the center of the chassis is a 50 W brushless DC motor with an off-the-shelf electronic speed controller and a 3-blade fixed-pitch propeller capable of producing more than 3 N of thrust. Embedded in the chassis is a Lithium-Ion Polymer battery that is capable of powering both the motors and the electronics for up to 5 min of flight. All modules are identical except for the spin direction (or handedness) of their propeller, where there are two possibilities: clockwise (CW) and counter-clockwise (CCW). This is necessary to cancel the aerodynamic torques in trimmed flight.

2.4. Sensing, communication and computation

The electronics were custom designed to meet all the on-board sensing, communication, and computation requirements. Each module comes equipped with a 3-axis rate gyro for measuring angular rates and a pressure sensor for measuring altitude. Bi-directional inter-module communication is accomplished using

infrared transceivers mounted to each side of the module. An ARM7 core microcontroller handles all the required computation needed for estimation and control.

3. Modeling

The DFA has two distinct modes of operation: (1) driving and (2) flying. This requires two different models which are discussed in Sections 3.1 and 3.2, respectively.

3.1. Kinematic drive model

Since the modules drive on the ground with relatively low velocities, dynamic effects that act on the system may be neglected. For this reason, the drive model considers only the kinematics of a rigid body with three independently-driven omni wheels.

The module's body coordinate frame M coincides with the geometric center of the module and follows a right-handed coordinate system, where the x-axis is orthogonal to a side of the module and the z-axis points upward, see Fig. 3. The transformation matrix $\mathbf{J}$, which maps the module's velocity $\dot{\zeta} = (V_x, V_y, \dot{\theta})$ in the module's body coordinate frame to wheel velocities $\mathbf{v} = (v_1, v_2, v_3)$ for an omni wheel vehicle, has been developed in previous work and is only summarized here [10]:

$$\mathbf{v} = \mathbf{J}\dot{\zeta}, \tag{1}$$

where

$$\mathbf{J} = \begin{bmatrix} -\frac{\sqrt{3}}{2} & \frac{1}{2} & r_w \\ 0 & -1 & r_w \\ \frac{\sqrt{3}}{2} & \frac{1}{2} & r_w \end{bmatrix}$$

and r_w is the lateral distance from the center of the wheel to the center of the module, see Fig. 3.

3.2. Dynamic flight model

The full flight dynamics of the DFA can be quite complex if effects like the flexibility of the propellers, aerodynamic effects of the rotor duct, and the forces that keep the modules together are considered [11–18]. As a first step, the system is modeled as a rigid body without any compliant inter-module connections, incorporating a force and torque generation process at each module around the hovering equilibrium. This will be shown to be adequate for the purpose of hover control in Section 5.

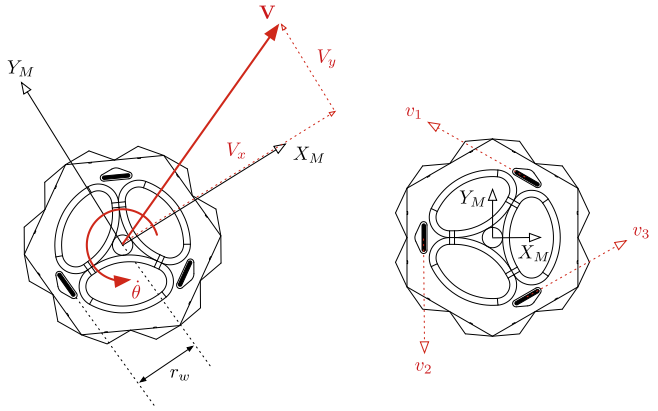

Fig. 3. The body coordinate frame M of a DFA module coincides with the geometric center of the module and follows a right-handed coordinate system, where the x-axis is orthogonal to a side of the module and the z-axis points upward. The module is driven by three independently-driven omni wheels with wheel velocities $\mathbf{v} = (v_1, v_2, v_3)$, which can be transformed to the module's velocity $\dot{\zeta} = (V_x, V_y, \dot{\theta})$.

3.2.1. Flight dynamics

The DFA's body coordinate frame B coincides with the array's center of mass and is oriented along the principal axes of rotation. Module i is located at coordinates (x_i, y_i) with respect to this body coordinate frame. A sequence of three rotations described by Euler angles α, β, γ acting along the z-, y-, x-axis in this order describe the orientation of the DFA's body coordinate frame with respect to the inertial coordinate frame O.

The altitude and attitude of the DFA can be controlled by varying the force (or thrust) f_i and torque τ_i produced by each module, see Fig. 4; how these control inputs are generated will be described later. The total thrust generated by N modules is the sum of all thrusts produced by each module, $F = \sum_{i=1}^{N} f_i$. The rolling torque is the sum of all thrusts acting along the moment arm y_i, $T_\gamma = \sum_{i=1}^{N} y_i f_i$. Similarly, the pitching torque is the sum of all thrusts acting along the moment arm x_i, $T_\beta = -\sum_{i=1}^{N} x_i f_i$. The yawing torque is the sum of all reaction torques produced by each module; it will be shown that the torque can be accurately modeled as a linear function of thrust. Hence, the yawing torque can be expressed as $T_\alpha = \sum_{i=1}^{N} c_i f_i$, where the sign of c_i depends on the propeller's handedness.

Transforming the total thrust vector F to the inertial coordinate frame results in a translational component of force along each axis. The translational accelerations $\ddot{x}$ and $\ddot{y}$ in the inertial coordinate frame is a consequence of a pitch β and roll γ rotation, respectively. Since the system is being modeled around the equilibrium, small angles are used to approximate the rotation in roll γ and pitch β. However, the rotation in yaw α is not assumed to be small. The following set of equations summarize the dynamics of the array to first-order, except for the yaw angle α:

$$Nm\ddot{x} = (\beta \cos\alpha + \gamma \sin\alpha) \sum_{i=1}^{N} f_i, \tag{2}$$

$$Nm\ddot{y} = (\beta \sin\alpha - \gamma \cos\alpha) \sum_{i=1}^{N} f_i, \tag{3}$$

$$Nm\ddot{z} = \sum_{i=1}^{N} f_i - Nmg, \tag{4}$$

$$I_x\ddot{\gamma} = \sum_{i=1}^{N} y_i f_i, \tag{5}$$

$$I_y\ddot{\beta} = -\sum_{i=1}^{N} x_i f_i, \tag{6}$$

$$I_z\ddot{\alpha} = \sum_{i=1}^{N} c_i f_i, \tag{7}$$

where Nm is the total mass of the array, (I_x, I_y, I_z) are the principal mass moments of inertia, and g is the acceleration constant due to gravity.

Assuming that the array configuration is relatively circular and letting ℓ denote the characteristic length of a module, then $\ell\sqrt{N}/2$ is comparable to the radius of the array. It follows that the principal mass moments of inertia can be written as the following:

$$I_x = \epsilon_x \frac{Nm}{4} \left(\frac{\ell\sqrt{N}}{2}\right)^2, \tag{8}$$

$$I_y = \epsilon_y \frac{Nm}{4} \left(\frac{\ell\sqrt{N}}{2}\right)^2, \tag{9}$$

$$I_z = \epsilon_z \frac{Nm}{2} \left(\frac{\ell\sqrt{N}}{2}\right)^2, \tag{10}$$

where $(\epsilon_x, \epsilon_y, \epsilon_z)$ capture the mass distribution of the array. If the configuration of the array is full, like a disk, $(\epsilon_x, \epsilon_y, \epsilon_z)$ are expected

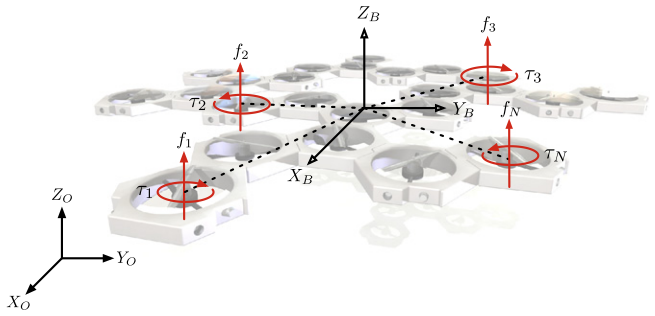

Fig. 4. The body coordinate frame B of the array is chosen to coincide with the array's center of mass and is aligned with the principal axes of rotation. The altitude and attitude of the DFA can be controlled by varying the force f_i and torque τ_i produced by each module.

to be close to 1. In reality, the configuration of the array may be sparse due to unpredictable docking constraints. In such a case, the values of $(\epsilon_x, \epsilon_y, \epsilon_z)$ are expected to be greater than 1.

The equations of motion are normalized using the following variables in order to gain some intuition on how the size of the array affects flight dynamics:

$$\hat{x}_i = \frac{x_i}{\frac{\ell\sqrt{N}}{2}}, \quad \hat{y}_i = \frac{y_i}{\frac{\ell\sqrt{N}}{2}}, \quad \hat{c}_i = \frac{c_i}{\ell}, \quad A_i = \frac{f_i}{m}, \tag{11}$$

where $\hat{x}_i$ and $\hat{y}_i$ are normalized position coordinates and are at most on the order of 1 for a circular array, $\hat{c}_i$ is the normalized force to torque conversion constant and is expected to be much less than 1, and A_i is the normalized thrust in units of acceleration.

The normalized thrust A_i can be broken down into its components, $A_i = \overline{A}_i + a_i$, where $\overline{A}_i$ is the normalized thrust required to establish the hovering equilibrium and a_i is the normalized control input. In the special case where there are an equal number of CW and CCW modules in the array, one can set $\overline{A}_i = g$. In general, however, the system may be overactuated with an unequal number of CW and CCW modules. In this case, one can choose the values of $\overline{A}_i$ via least squares, or any other suitable method.

The following set of equations summarize the normalized and linearized equations of motion about hovering equilibrium:

$$\ddot{x} = \frac{1}{N}(\beta\cos\alpha + \gamma\sin\alpha)\sum_{i=1}^{N} a_i, \tag{12}$$

$$\ddot{y} = \frac{1}{N}(\beta\sin\alpha - \gamma\cos\alpha)\sum_{i=1}^{N} a_i, \tag{13}$$

$$\ddot{z} = \frac{1}{N}\sum_{i=1}^{N} a_i, \tag{14}$$

$$\widehat{I}_x\ddot{\gamma} = \frac{1}{N}\sum_{i=1}^{N} \hat{y}_i a_i, \tag{15}$$

$$\widehat{I}_y\ddot{\beta} = -\frac{1}{N}\sum_{i=1}^{N} \hat{x}_i a_i, \tag{16}$$

$$\widehat{I}_z\ddot{\alpha} = \frac{1}{N}\sum_{i=1}^{N} \hat{c}_i a_i, \tag{17}$$

where

$$\widehat{I}_x = \frac{\epsilon_x\ell\sqrt{N}}{8}, \quad \widehat{I}_y = \frac{\epsilon_y\ell\sqrt{N}}{8}, \quad \widehat{I}_z = \frac{\epsilon_z\ell N}{8}. \tag{18}$$

It can be seen from (14) that the maximum vertical acceleration $\ddot{z}$ is independent of N. On the other hand, by substituting (18) into (15)–(17) and rearranging, it can be shown that the maximum accelerations in roll $\ddot{\gamma}$ and in pitch $\ddot{\beta}$ decrease by a factor of $\sqrt{N}$, while the maximum acceleration in yaw $\ddot{\alpha}$ decreases by a factor of N.

Disregarding the x and y translational components of motion, the DFA requires at least four modules to hover; four is the minimum number of control inputs a_i needed to control the four remaining degrees of freedom (14)–(17). This, however, is only a necessary condition and not a sufficient condition to keep the array hovering. For example, four modules lined together in a row would not be linearly stable in attitude; the system would either be controllable in roll and not in pitch, or vice versa.

3.2.2. Force and torque generation

The module's force-torque generation unit (i.e. motor controller, brushless DC motor, battery, propeller, and rotor duct) is treated as a black box model. The input to this system is a pulse-width modulation (PWM) duty cycle D that effectively controls the angular velocity of the rotor. Battery voltage can also be considered as an input to the system, however the effects of voltage on the dynamics of the system are ignored since the nominal voltage of Lithium-Ion Polymer batteries is relatively constant over the battery cycle [19,20]. The force-torque characteristics that are described here assume the nominal voltage case around the equilibrium thrust. The output from this system is both the generated force and torque of the module. Torque is a result of the imparted rotational flow and change in angular momentum of the rotor.

Force and torque measurements were made at various duty cycles around the equilibrium thrust. The force experienced by a module is dominated by the thrust of the rotor. Experimental results show that thrust and duty cycle can be approximated by an affine relationship, while the torque resulting from the rotor's drag can be approximated as a linear function of thrust, see Fig. 5a and b. Recall that this thrust-torque relationship was used in (7) and is expressed in the following:

$$\tau_i = cf_i, \tag{19}$$

where $c = \pm 1.13 \times 10^{-2}$ m; recall that the sign of c depends on the propeller's handedness. Other experiments demonstrated that the effect of torque produced by the rate of change in angular momentum of the rotor to be negligible.

Motivated by the results in Fig. 5a and b, the transfer function G_f which relates the input desired thrust $f(D)$ to the output thrust was modeled as a linear time-invariant system. The transfer function that was obtained from the Bode plot of the thrust response, shown in Fig. 6, was found to approximate a first-order system:

$$G_f(s) = \frac{\omega}{s+\omega}, \tag{20}$$

where $\omega = 14.3$ rad/s.

4. Driving strategy

At the start of each cycle, a number of DFA modules will be scattered randomly across the floor. Without any prior knowledge about the environment, the module's objective will be to dock with its peers in preparation for coordinated flight. Although the assembly process could be controlled to achieve a particular array configuration, a decision was made to let the self-assembly process occur at random with the intent that a new configuration is flown each time. The docking strategy summarized here is one of many possibilities that increases the likelihood of modules finding one another.

Consider an overhead light source as the only environmental feature detectable by each module via a single on-board photodiode. This photodiode along with encoder odometry will be the only source of information used for pose estimation. Modules will be

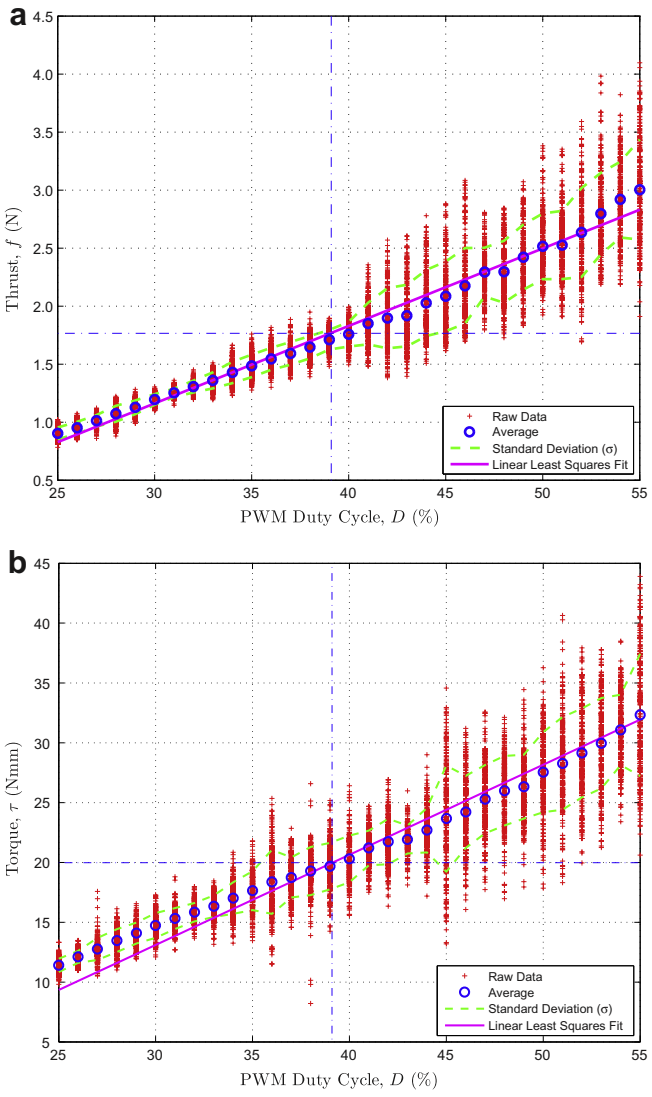

Fig. 5. Force and torque values were measured with a 6-axis force-torque strain gauge load cell at various PWM duty cycles near the hovering equilibrium (approximately D = 39%), and is denoted by the pair of dashed-dotted horizontal and vertical lines. At each duty cycle, 500 measurements were made over a period of 5 s. (a) A linear least squares fit of the data relating thrust f to PWM duty cycle D at nominal voltage results in the function $f(D) = 6.68\times10^{2}D - 8.41\times10^{-1}$. (b) A linear least squares fit to the function $cf(D)$ of the data relating torque τ to PWM duty cycle D at nominal voltage results in the function $\tau(D) = 1.13\times10^{-2}f(D)$.

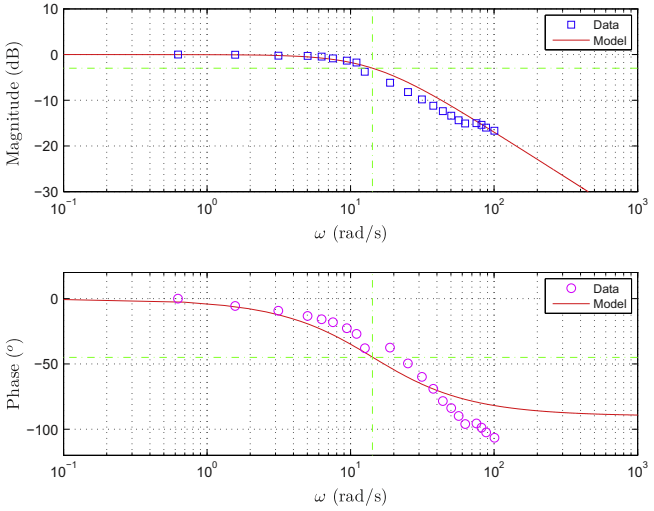

Fig. 6. The Bode plot of the flight motor thrust response is shown here to approximate a first-order system. A sinusoidal varying PWM duty cycle, with an offset equivalent to the hovering thrust and an amplitude equivalent to 0.5 N, was commanded to the system. Force and torque measurements were made using a 6-axis force-torque strain gauge load cell. The dash-dotted lines in the plots indicate the magnitude and phase at −3 dB frequency, which is 14.3 rad/s. Note that at high frequencies the measured phase diverges from the model; this is due to unmodeled dynamics, such as delays.

able to move around a prescribed circular region as defined by the cone of illumination from the overhead light source, see Fig. 7. A user-defined light intensity threshold will force a module into one of two states: (1) within the circular region and (2) outside the circular region.

The goal of each module will be to drive towards the center of the circular region and arbitrarily dock with its peers. Modules will initially drive in random directions. Once a module crosses the boundary of the circular region at three different locations, it will be able to use these three data points to estimate the center of the circle and to drive towards it. Modules may randomly connect during the data point collection process, during which they may share information to improve their common estimate of the circular region [21,22]. Depending on their estimate, they will coordinate to either continue exploration, or to move towards the center.

A 2D simulator using the Box2D physics engine [23] is currently being developed to experiment with this and other docking strategies, see Fig. 8. It will be used to obtain array configuration statistics, which will be needed to determine the typical mass distribution parameter values $(\epsilon_x, \epsilon_y, \epsilon_z)$ required for testing various control strategies and analyzing their performance.

5. Flight control

This section presents an easily tunable strategy for hover control based on physical parameters of the DFA and compares its performance and tradeoffs to that of an $\mathscr{H}_2$ controller. The derivation of this control strategy is generalized, and assumes full state feedback of the system. It is assumed that an estimator is used to obtain the state of the system [24,25].

5.1. Control strategy

Starting with the dynamic model of the DFA that was developed in the previous section, and ignoring the degrees of freedom along the x and y axes, the normalized and linearized equations of

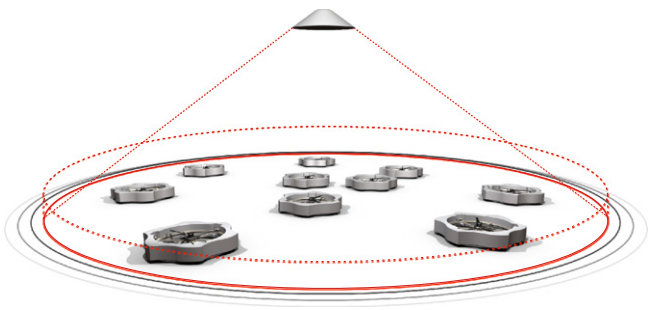

Fig. 7. The DFA modules may be randomly scattered across a circular area defined by the cone of illumination from an overhead light source. The perimeter of this circular region can be adjusted by varying the light intensity, the height of the lamp, the aperture of the light source, and/or the intensity threshold of the module's photodiode. The modules can use this light source as a means of localization, which can in turn assist with self-assembly.

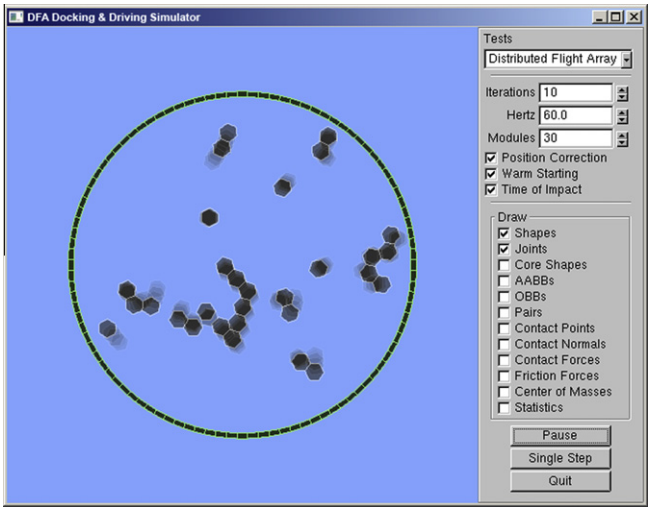

Fig. 8. A docking and driving simulator is being developed using the Box2D physics engine. The simulator will be used to obtain array configuration statistics, which will be needed for testing various control strategies and analyzing their performance.

motion about the hovering equilibrium (14)–(17) can be more compactly expressed as

$$\mathbf{M}\ddot{\mathbf{s}} = \mathbf{P}^T\mathbf{a}, \tag{21}$$

where

$$\begin{aligned}\mathbf{M} &= \mathrm{diag}(1, \widehat{I}_x, \widehat{I}_y, \widehat{I}_z),\\ \mathbf{s} &= [z, \gamma, \beta, \alpha]^T,\\ \mathbf{a} &= [a_1, \ldots, a_N]^T.\end{aligned}$$

The matrix $\mathbf{P} \in \mathbb{R}^{N\times 4}$ contains information pertaining to the configuration of the array and can be written as

$$\mathbf{P} = [\mathbf{p}_z, \mathbf{p}_\gamma, \mathbf{p}_\beta, \mathbf{p}_\alpha], \tag{22}$$

where

$$\mathbf{p}_z = \frac{1}{N}[1, \ldots, 1]^T, \qquad \mathbf{p}_\gamma = \frac{1}{N}[\hat{y}_1, \ldots, \hat{y}_N]^T,$$
$$\mathbf{p}_\beta = -\frac{1}{N}[\hat{x}_1, \ldots, \hat{x}_N]^T, \quad \mathbf{p}_\alpha = \frac{1}{N}[\hat{c}_1, \ldots, \hat{c}_N]^T.$$

Consider the control strategy of the following form:

$$\mathbf{a} = \mathbf{Q}f(z, \dot{z}, \gamma, \dot{\gamma}, \beta, \dot{\beta}, \alpha, \dot{\alpha}), \tag{23}$$

where

$$\begin{aligned}\mathbf{Q} &= [\mathbf{q}_z, \mathbf{q}_\gamma, \mathbf{q}_\beta, \mathbf{q}_\alpha],\\ \mathbf{f} &= [f_z(z, \dot{z}), f_\gamma(\gamma, \dot{\gamma}), f_\beta(\beta, \dot{\beta}), f_\alpha(\alpha, \dot{\alpha})]^T,\end{aligned}$$

and where the $f(\cdot)$ are arbitrary functions to be determined.

The objective is to decouple the degrees of freedom. This can be accomplished by designing $\mathbf{Q} \in \mathbb{R}^{N\times 4}$ such that $\mathbf{P}^T\mathbf{Q} = \mathbf{I}_4$, resulting in the following diagonal system:

$$\ddot{z} = f_z(z, \dot{z}), \tag{24}$$
$$\widehat{I}_x\ddot{\gamma} = f_\gamma(\gamma, \dot{\gamma}), \tag{25}$$
$$\widehat{I}_y\ddot{\beta} = f_\beta(\beta, \dot{\beta}), \tag{26}$$
$$\widehat{I}_z\ddot{\alpha} = f_\alpha(\alpha, \dot{\alpha}). \tag{27}$$

Notice that the system is over-determined for an array with more than four modules.

Due to the coordinate system described in Section 3.2.1, $\mathbf{p}_z$, $\mathbf{p}_\gamma$, and $\mathbf{p}_\beta$ are orthogonal. If there are an equal number of CW and CCW modules, then $\mathbf{p}_z$ and $\mathbf{p}_\alpha$ are also orthogonal. In what follows, consider an equal number of CW and CCW modules; the results can readily be generalized.

Let $\mathbf{Q} = \mathbf{P}\mathbf{D}\overline{\mathbf{Q}}$, where

$$\mathbf{D} = \mathrm{diag}\left(\frac{1}{\|\mathbf{p}_z\|^2}, \frac{1}{\|\mathbf{p}_\gamma\|^2}, \frac{1}{\|\mathbf{p}_\beta\|^2}, \frac{1}{\|\mathbf{p}_\alpha\|^2}\right)$$

and $\|\cdot\|$ is the Euclidean norm.

Multiplying $\mathbf{P}^T$ on both sides yields:

$$\begin{aligned}\mathbf{I}_4 = \mathbf{P}^T\mathbf{Q} &= \mathbf{P}^T\mathbf{P}\mathbf{D}\overline{\mathbf{Q}}\\ &= \begin{bmatrix} \|\mathbf{p}_z\|^2 & 0 & 0 & 0\\ 0 & \|\mathbf{p}_\gamma\|^2 & 0 & \mathbf{p}_\gamma^T\mathbf{p}_\alpha\\ 0 & 0 & \|\mathbf{p}_\beta\|^2 & \mathbf{p}_\beta^T\mathbf{p}_\alpha\\ 0 & \mathbf{p}_\alpha^T\mathbf{p}_\gamma & \mathbf{p}_\alpha^T\mathbf{p}_\beta & \|\mathbf{p}_\alpha\|^2 \end{bmatrix}\mathbf{D}\overline{\mathbf{Q}}\\ &= \begin{bmatrix} 1 & 0 & 0 & 0\\ 0 & 1 & 0 & e_1\\ 0 & 0 & 1 & e_2\\ 0 & e_3 & e_4 & 1 \end{bmatrix}\overline{\mathbf{Q}},\end{aligned} \tag{28}$$

where

$$e_1 = \frac{\mathbf{p}_\gamma^T\mathbf{p}_\alpha}{\|\mathbf{p}_\alpha\|^2}, \quad e_2 = \frac{\mathbf{p}_\beta^T\mathbf{p}_\alpha}{\|\mathbf{p}_\alpha\|^2},$$
$$e_3 = \frac{\mathbf{p}_\alpha^T\mathbf{p}_\gamma}{\|\mathbf{p}_\gamma\|^2}, \quad e_4 = \frac{\mathbf{p}_\alpha^T\mathbf{p}_\beta}{\|\mathbf{p}_\beta\|^2}.$$

It can readily be shown that

$$\overline{\mathbf{Q}} = \begin{bmatrix} 1 & 0\\ 0 & \overline{\overline{\mathbf{Q}}} \end{bmatrix}, \tag{29}$$

where

$$\overline{\overline{\mathbf{Q}}} = \frac{1}{1 - (e_2e_4 + e_3e_1)}\begin{bmatrix} 1 - e_2e_4 & e_1e_4 & -e_1\\ e_2e_3 & 1 - e_3e_1 & -e_2\\ -e_3 & -e_4 & 1 \end{bmatrix}.$$

In the special case where there are a large number of CW and CCW modules that are uniformly distributed in the array, $\mathbf{p}_\gamma$ and $\mathbf{p}_\beta$ are approximately orthogonal to $\mathbf{p}_\alpha$. This can be made mathematically precise, but the intuition is straightforward: a roll or pitch action employs roughly the same number of CW and CCW modules, and thus the net yawing torque is zero. The result of having a large number of modules N in the array is that $e_i \to 0$, which results in $\overline{\overline{\mathbf{Q}}} \to \mathbf{I}_3$ and $\mathbf{Q} \to \mathbf{P}\mathbf{D}$. One could then use the following decoupling strategy:

$$\mathbf{q}_z = \frac{\mathbf{p}_z}{\|\mathbf{p}_z\|^2}, \quad \mathbf{q}_\gamma = \frac{\mathbf{p}_\gamma}{\|\mathbf{p}_\gamma\|^2},$$
$$\mathbf{q}_\beta = \frac{\mathbf{p}_\beta}{\|\mathbf{p}_\beta\|^2} \quad \mathbf{q}_\alpha, = \frac{\mathbf{p}_\alpha}{\|\mathbf{p}_\alpha\|^2}.$$

It can be shown that the above elements of $\mathbf{Q}$ do not scale with N, and thus this decoupling strategy is independent of N. Moreover, this strategy has the desirable property of minimizing the inter-module shear stresses in the array resulting from pitch and roll errors. This can readily be seen by substituting $\mathbf{Q}$ into the control strategy (23) and analyzing the resulting expression; the control input a_i increases linearly the further away a module is from the center of mass. As a result, the shear stress acting between two modules is minimized. This is an important feature because too much shear stress would cause the module(s) to break away from the array.

This control strategy only works if both **P** and $(\widehat{I}_x, \widehat{I}_y, \widehat{I}_z)$ are known. Assuming that all modules are identical and that the mass and mass moments of inertia are given, then both of these parameters can be computed if the position and the propeller's handedness for each module is known. It follows that this is the only information that needs to be communicated across the array before taking flight.

Now that the control strategy has been decoupled, one can consider each degree of freedom separately. For example, the following functions can be chosen:

$$f_z(z,\dot{z}) = -2\omega_z\zeta_z\dot{z} - \omega_z^2(z - z_d), \tag{30}$$

$$f_\gamma(\gamma,\dot{\gamma}) = -\widehat{I}_x(2\omega_\gamma\zeta_\gamma\dot{\gamma} + \omega_\gamma^2\gamma), \tag{31}$$

$$f_\beta(\beta,\dot{\beta}) = -\widehat{I}_y(2\omega_\beta\zeta_\beta\dot{\beta} + \omega_\beta^2\beta), \tag{32}$$

$$f_\alpha(\alpha,\dot{\alpha}) = -\widehat{I}_z(2\omega_\alpha\zeta_\alpha\dot{\alpha} + \omega_\alpha^2\alpha), \tag{33}$$

where z_d represents the desired hovering altitude and each degree of freedom is a second-order system with two sets of tuning parameters: (1) the natural frequencies $(\omega_z,\omega_\gamma,\omega_\beta,\omega_\alpha)$ and (2) the damping ratios $(\zeta_z,\zeta_\gamma,\zeta_\beta,\zeta_\alpha)$. The tuning of these two sets of parameters will depend on the DFA's mass moment of inertia, which is affected by the size and configuration of the array. Recall that the effect due to the size of the array N is more pronounced in the yaw degree of freedom than in roll and/or pitch by a factor of $\sqrt{N}$, see Section 3.2.1.

Be aware that this control strategy uses normalized thrust as the control input, which is in fact indirectly generated by the DFA module as described in Section 3.2.2. Thrust dynamics and saturation of the control inputs should be considered. Time-scale separation is needed between the desired dynamics of the system and the rotor dynamics. A way to achieve this is to invert the transfer function G_f over a desired frequency range, enough to achieve time-scale separation.

5.2. Simulation

The control strategy described here has been simulated in MATLAB for random array configurations consisting of 4 and up to 20 modules, see Figs. 9 and 10. The state of the array is obtained locally from the onboard sensors of each module. That is to say that no information is passed between modules, resulting in a completely decentralized control scheme; altitude is obtained from the pressure sensor, angular rates are measured using the rate gyros, and these are integrated to obtain the Euler angles of the array in flight. Simulations take into account measurement and process noise derived from physical experiments and the motor model described in Section 3.2.2.

5.3. Performance

A quantitative comparison was made between the easily tunable control strategy described previously and an $\mathscr{H}_2$ controller. A generalized plant $G(h)$, which includes the plant model based on the configuration of the array seen in Fig. 10a, measurement and process noise derived from physical experiments, and weights h on the states (z,γ,β,α) and on the normalized control input **a** were used for the purpose of this comparison, see Fig. 11a and b. The $\mathscr{H}_2$ optimal control problem is to find a stabilizing controller $K_{\mathscr{H}_2}$ that minimizes the $\mathscr{H}_2$ norm (i.e. the expected root mean square value of the output **e** in response to white noise excitation [26]) of the closed loop system. The optimal $\mathscr{H}_2$ controller was synthesized in MATLAB by setting the state weights $(h_z,h_\gamma,h_\beta,h_\alpha)$ to a reasonable set of constant values and adjusting the normalized control input weight h_a subject to not saturating the thrusts produced by the rotors. By doing this, an $\mathscr{H}_2$ norm of 5.385 was computed. See

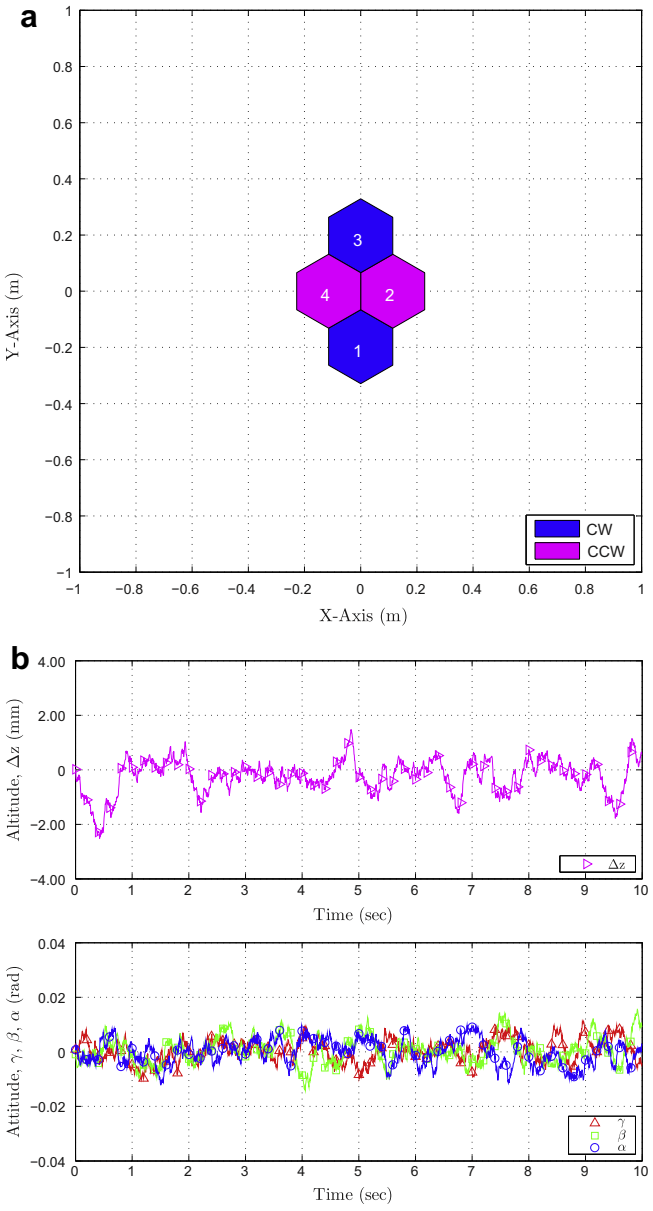

Fig. 9. Simulation results around the hovering equilibrium using a decentralized controller on a 4-module array configuration, where the natural frequencies were set to $(\omega_z,\omega_\gamma,\omega_\beta,\omega_\alpha)$=(9.016, 9.021, 9.021, 9.016) rad/s and the damping ratios were set to $(\zeta_z,\zeta_\gamma,\zeta_\beta,\zeta_\alpha)$=(1,1,1,1). An $\mathscr{H}_2$ norm of 5.1 was obtained for this particular scenario. (a) 4-Module array configuration. (b) Simulation results around the hovering equilibrium using a decentralized controller.

Fig. 12 for a simulation of the output states of the $\mathscr{H}_2$ controller around the hovering equilibrium.

The same generalized plant $G(h)$ and weights h were used with the easy to tune controller $K(p)$, see Fig. 11b. Recall from (30)–(33) that the control tuning parameters p are the natural frequencies $(\omega_z,\omega_\gamma,\omega_\beta,\omega_\alpha)$ and the damping ratios $(\zeta_z,\zeta_\gamma,\zeta_\beta,\zeta_\alpha)$. For this comparison, the damping ratios were fixed to a constant value of *1* and the natural frequencies were adjusted to minimize the $\mathscr{H}_2$ norm via a gradient descent method; this resulted in a norm of 5.529. Even with just four tuning parameters $(\omega_z,\omega_\gamma,\omega_\beta,\omega_\alpha)$, this controller comes to within 3% of the optimal controller for this particular scenario. In addition to its good performance, this control strategy is well structured and transparent; the degrees of freedom are decoupled, which results in a straightforward design and method for tuning this controller in comparison with the non-intuitive $\mathscr{H}_2$ controller.

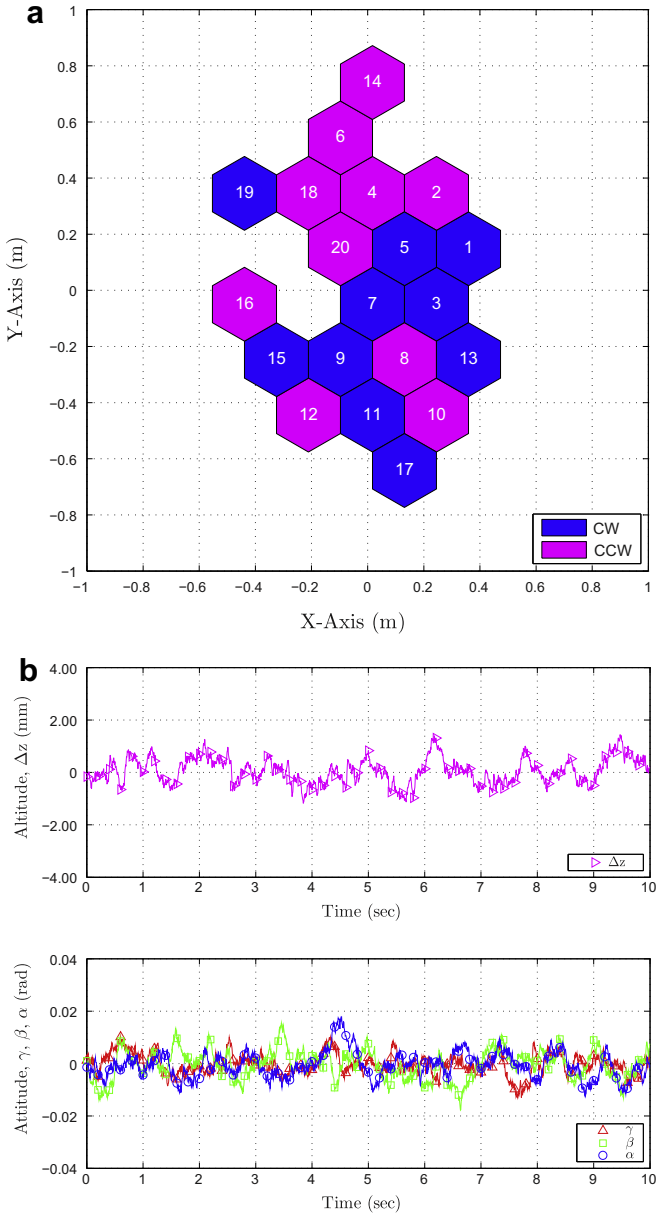

Fig. 10. Simulation results around the hovering equilibrium using a decentralized controller on a 20-module array configuration, where the natural frequencies were set to $(\omega_z,\omega_\gamma,\omega_\beta,\omega_\alpha)$= (9.012, 9.020, 9.020, 9.013) rad/s and the damping ratios were set to $(\zeta_z,\zeta_\gamma,\zeta_\beta,\zeta_\alpha)$ = (1,1,1,1). An $\mathscr{H}_2$ norm of 5.529 was obtained for this particular scenario. (a) 20-Module array configuration. (b) Simulation results around the hovering equilibrium using a decentralized controller.

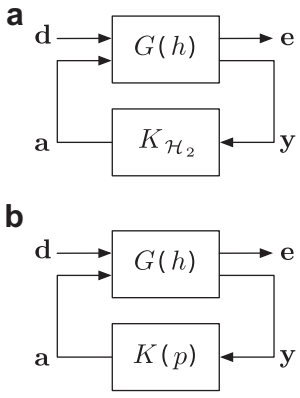

Fig. 11. Block diagrams representing the generalized plant $G(h)$ with feedback from the H_2 controller, $K_{\mathscr{H}_2}$, and the controller described in Section 5.1, $K(p)$. The signals for these systems are: the normalized control input $\mathbf{a} = [a_1, \ldots, a_N]^T$ in units of acceleration; the disturbances $\mathbf{d} = [d_1, \ldots, d_N]^T$, where d_i is a vector of process and measurement noises affecting module i; the error signals $e = [z, h_\gamma\gamma, h_\beta\beta, h_\alpha\alpha, h_a\mathbf{a}]^T$, which are the weighted states and control input that are to be minimized in the $\mathscr{H}_2$ sense; and the states of the array $(z,\gamma,\beta,\alpha,\dot{z},\dot{\gamma},\dot{\beta},\dot{\alpha})$ corrupted by noise y. (a) Block diagram of the system with $K_{\mathscr{H}_2}$ feedback. (b) Block diagram of the system with $K(p)$.

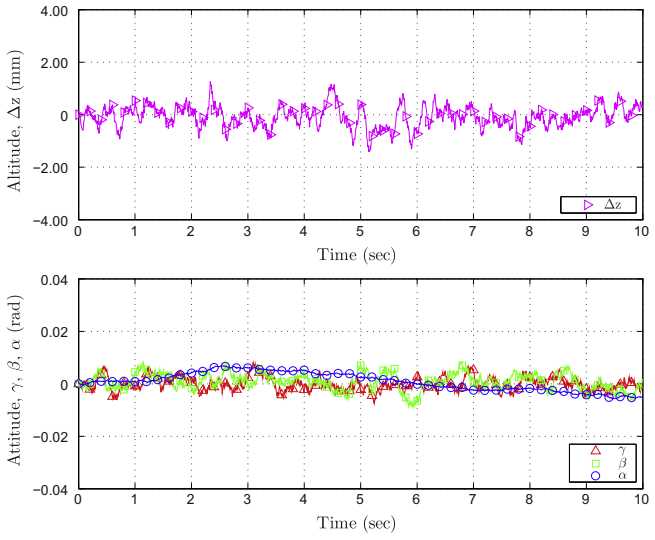

Fig. 12. Simulation results around the hovering equilibrium using an $\mathscr{H}_2$ controller on the 20-module array configuration as seen in Fig. 10a. An $\mathscr{H}_2$ norm of 5.385 was obtained for this particular scenario.

6. Experiments

Three important aspects of the DFA were demonstrated in order to verify its feasibility, see Video 2 in Appendix A: (1) docking, (2) driving, and (3) flying. Each one in sequence is a prerequisite to the next, and therefore each is needed to achieve the end goal of coordinated flight.

6.1. Docking

A variety of experiments were performed to test the module's ability to dock. Based on experimental results, two modules have the highest probability of successfully docking when one is rotating and another is translating along converging trajectories, see Fig. 13. Although docking will be sufficiently random, this is an important observation to consider when developing a driving strategy to ensure that modules readily dock together [27,28].

6.2. Driving

Two modules were driven together and used to demonstrate maneuvers which would otherwise be impossible without the use of omni wheels or a steering mechanism; omni wheels increase the degree of maneuverability and in turn eases docking constraints. The pair of modules performed pirouettes along a circular trajectory, i.e. the pair rotated around their combined center while both modules followed a 1.3 m diameter circular trajectory in the direction opposite to their rotation.

A camera-based motion capture system was used to measure the performance of this pirouette maneuver, which performed very well considering that the maneuver was carried out open

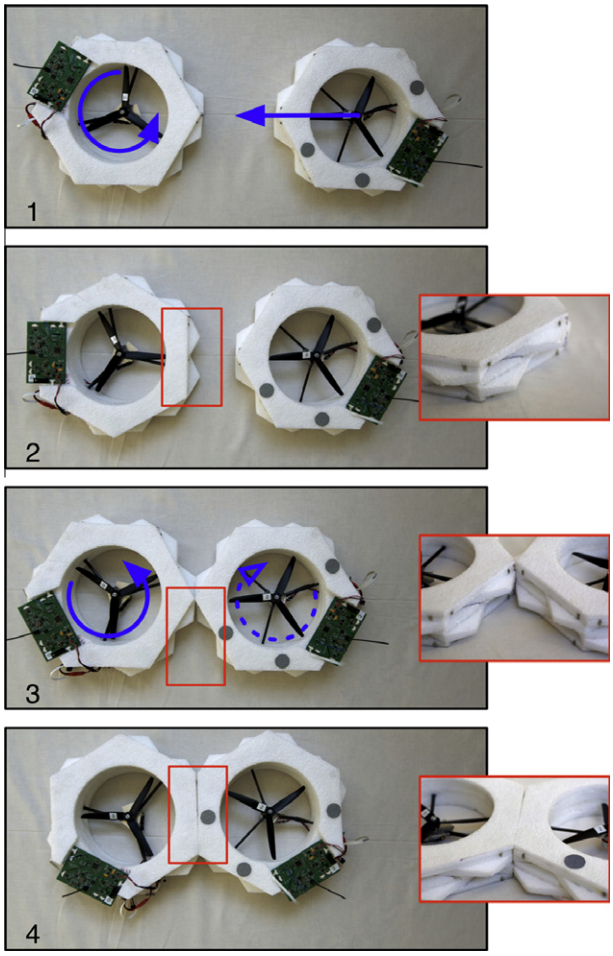

Fig. 13. In frames 1–2 of this docking image sequence, the left module rotates counter-clockwise while the right module drives forward, towards the rotating module. In frame 3, the modules collide. The left module continues to rotate counter-clockwise and due to its protruding features it induces a clockwise rotation in the right module, which continues to drive forward. The modules finally dock together, making a solid connection in frame 4.

loop, see Fig. 14 [29]. The pair was able to meet the desired trajectory with relatively good accuracy and precision while performing a 1.3 m diameter orbit over six times. This repeatability adds weight to the method of module fabrication and the chosen driving surface.

6.3. Flying

The linear model presented in Section 3.2.1 and the results gathered from simulating the decentralized controller described in Section 5.2 were verified by testing this control strategy on the DFA in the array configuration shown in Fig. 2a. Preliminary results established that the pressure sensor performed poorly and provided imprecise altitude measurements; sudden changes to the environment, like the opening and closing of a room door, resulted in a dramatic change of pressure. Future revisions of the DFA will address this issue with sensors that are not as sensitive to changes in the environment, such as optical time-of-flight sensors. For this reason altitude control was excluded from the experiments. Moreover, yaw control was intentionally left out to simplify the analysis. As a result, experiments were made using only roll and pitch as feedback to the controller, see (31) and (32).

Before taking flight, the modules synchronized via infrared transceivers and removed all sensor bias over a 5 s initialization sequence. Rate gyro measurements were made at 200 Hz and the controller was operated at 60 Hz. The function f_z (30), which is the deviation around the hovering thrust in units of acceleration, was set to a very small value. A camera-based motion capture system was used to measure both the altitude and the attitude of the DFA during flight, see Fig. 15.

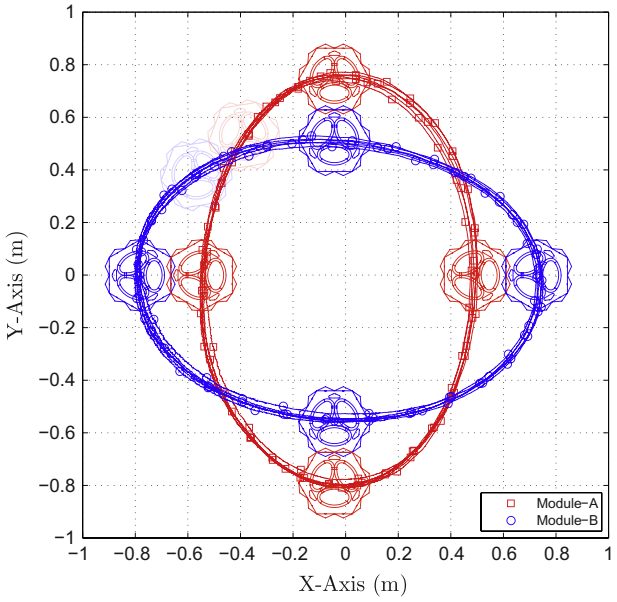

Fig. 14. The two set of trajectories in this plot represent the centers of two docked modules (A and B) during an open-loop pirouette driving maneuver, and demonstrates repeatability for over six orbits. The position of the modules were measured using a camera-based motion capture system.

The DFA was shown to fly successfully with roll and pitch control. The experimental results shown in Fig. 15b are comparable to the simulation results shown in Fig. 15a, thus verifying the utility of the linear model and the simulator.

One interesting and unexpected result was observed due to yaw being left uncontrolled: the DFA ascended in a spiraling motion, keeping its x and y position of climb within the perimeter of the spiral, and thus mitigating drift. This behaviour is in fact expected due to the sine and cosine terms seen in (2) and (3), assuming that roll γ and pitch β are non-zero, and that the magnitude of yaw α is increasing over time. This motivates the following constant yaw-rate control law:

$$f_\alpha(\dot{\alpha}) = -\widehat{I}_z \omega_\alpha(\dot{\alpha} - \dot{\alpha}_d), \tag{34}$$

where $\dot{\alpha}_d$ is the desired yaw-rate.

7. Conclusions and future work

This paper presented the Distributed Flight Array (DFA), a unique modular multi-rotor vehicle capable of autonomous self-assembly and coordinated flight. The initial prototype of the DFA has established its feasibility by demonstrating various important aspects of the system, including: docking, driving, and flying. Significant improvements are being made to the second revision of the DFA, which will result in a more robust platform and will enable coordinated driving and flying experiments on a larger scale, including non-symmetric flying configurations.

When there are more than four modules in the array, the system becomes overactuated, leading to some interesting questions on how resources should be optimally used in a distributed system. Questions like what type of array configurations lead to more stable flight, more aggressive maneuvers, or consume the least

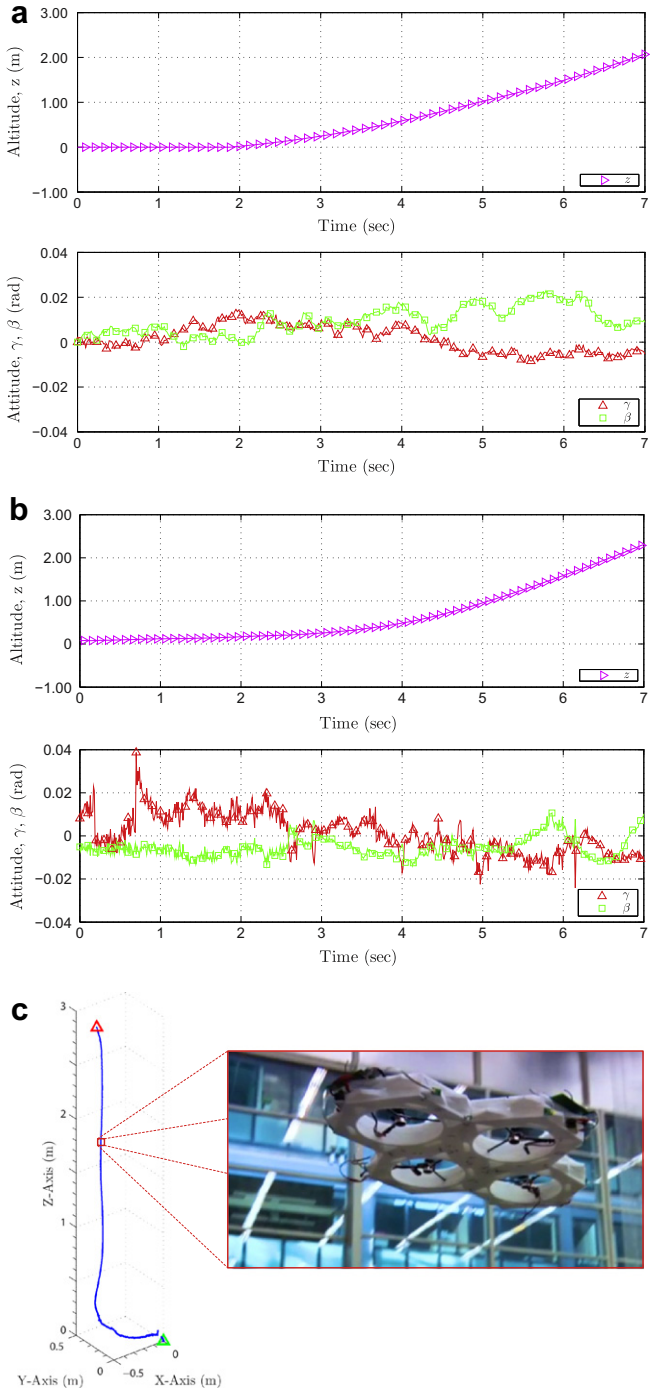

Fig. 15. Comparison of the results gathered from a simulation and an experimental attitude-controlled flight test without feedback on altitude and yaw. Experimental measurements were made using a camera-based motion capture system: (a) Simulated results for the 4-module array configuration seen in Fig. 9a without feedback on altitude and yaw, and using a decentralized controller, where the natural frequencies and damping ratios were set to $(\omega_\gamma,\omega_\beta)$ = (13,13) rad/s and $(\zeta_\gamma,\zeta_\beta)$ = (1,1), respectively. (b) Experimental results for the same 4-module array configuration and using the same controller that was used to obtain the simulation results shown in (a). (c) A plot of the 4-module array's 3D position relative to its take-off origin, obtained from experimental results.

amount of energy will be considered. Research challenges include quantifying the minimum amount of information that must be shared to achieve a particular level of performance. Other objectives include controlling the amount of inter-module shear stress in order to perform mid-air disassembly maneuvers. These results will be presented in future work.

Acknowledgments

The authors would like to thank the team of technicians, researchers, and students of the 2008–2009 *!And Yet it Moves* class at ETH Zurich for their contribution to the design and construction of the DFA modules (rev. 1). A special mention goes to Frédéric Bourgault, Daniel Burch, and Matthew Donovan, from the same institution, for their contribution to the design of the modules and thoughtful discussions. This research is supported by the Swiss National Science Foundation.

Appendix A. Supplementary data

Supplementary data associated with this article can be found, in the online version, at doi:10.1016/j.mechatronics.2010.08.003.

References

[1] Bernard M, Kondak K. Generic slung load transportation system using small size helicopters. In: Proceedings of the IEEE international conference on robotics and automation; 2009. p. 3258–64.
[2] Vance E. High hopes. Nature 2009;460:564–6.
[3] Yim M, Shen W, Salemi B, Rus D, Moll M, Lipson H, et al. Modular self-reconfigurable robot systems. IEEE Robot Automat Mag 2007;14(1):43–52.
[4] Klaptocz A, Nicoud J. Technology and fabrication of ultralight micro-aerial vehicles. New York: Springer-Verlag; 2009.
[5] Schafroth D, Bouabdallah S, Bermes C, Siegwart R. From the test benches to the first prototype of the muFly micro helicopter. J Intell Robot Syst 2009;54(1):245–60.
[6] Van Breugel F, Regan W, Lipson H. Demonstration of a passively stable, untethered flapping–hovering micro-air vehicle. IEEE Robot Automat Mag 2008;15:68–74.
[7] Bouabdallah S, Noth A, Siegwart R. PID vs LQ control techniques applied to an indoor micro quadrotor. In: Proceedings of the IEEE international conference on intelligent robots and systems, vol. 3; 2004. p. 2451–6.
[8] Bouix R, Viot P, Lataillade J. Polypropylene foam behaviour under dynamic loadings: strain rate, density and microstructure effects. Int J Impact Eng 2009;36(2):329–42.
[9] Lee Y, Park N, Yoon H. Dynamic mechanical characteristics of expanded polypropylene foams. J Cell Plast 2009;00:1–13.
[10] Agullo J, Cardona S, Vivancos J. Kinematics of vehicles with directional sliding wheels. Mech Mach Theory 1987;22(4):295–301.
[11] Lee J, Yee K, Oh S. Aerodynamic characteristic analysis of multi-rotors using a modified free-wake method. Trans Jpn Soc Aeronaut Space Sci 2009;52(177):168–79.
[12] Reed III W. Propeller-rotor whirl flutter: a state-of-the-art review. J Sound Vib 1966;4(3):526–30.
[13] Sacks AH, Burnell JA. Ducted propellers – a critical review of the state of the art. Prog Aerosp Sci 1962;3:85–135.
[14] Howell LL. Compliant mechanisms. Wiley-Interscience; 2001.
[15] Leishman JG. Principles of helicopter aerodynamics. 2nd ed. Cambridge University Press; 2006.
[16] McCormick B. Aerodynamics of V/STOL flight. Dover Publications; 1999.
[17] Weir RJ. Aerodynamic design considerations for a free-flying ducted propeller. In: AIAA atmospheric flight mechanics conference; 1988. p. 420–31.
[18] Bristeau PJ, Martin P, Salaün E, Petit N. The role of propeller aerodynamics in the model of a quadrotor UAV. In: Proceedings of the European control conference; 2009. p. 683–8.
[19] Nishi Y. Lithium ion secondary batteries; past 10 years and the future. J Power Sour 2001;100(1–2):101–6.
[20] Wakihara M. Recent developments in lithium ion batteries. Mater Sci Eng 2001;33(4):109–34.
[21] Fox D, Burgard W, Kruppa H, Thrun S. A probabilistic approach to collaborative multi-robot localization. Autonom Robot 2000;8(3):325–44.
[22] Shaw FW, Klavins E. Distributed estimation and control for stochastically interacting robots. In: IEEE conference on decision and control; 2008. p. 1895–901.
[23] Box2D Physics Engine; 2010. <http://www.box2d.org/> [accessed: 21.07.10].
[24] Ren W, Beard RW, Atkins EM. Information consensus in multivehicle cooperative control. IEEE Control Syst Mag 2007;27(2):71–82.
[25] Olfati-Saber R, Fax J, Murray R. Consensus and cooperation in networked multi-agent systems. Proc IEEE 2007;95(1):215–33.
[26] Skogestad S, Postlethwaite I. Multivariable feedback control: analysis and design. 2nd ed. John Wiley & Sons, Ltd.; 2005.
[27] Klavins E. Programmable self-assembly. IEEE Control Syst Mag 2007;27(4):43–56.
[28] Whitesides G, Grzybowski B. Self-assembly at all scales. Science 2002;295(5564):2418–21.
[29] Vicon; 2010. <http://www.vicon.com/> [accessed 21.07.10].